THE COMPENSATION STATE AND RING STRUCTURES OF LUNAR BASINS AS REVEALED BY GRAIL GRAVITY. Jeffrey C. Andrews-Hanna[1], Andrew M. Freed[2], James W. Head III[3], H. Jay Melosh[2], Gregory A. Neumann[4], Jason M. Soderblom[6], Mark A. Wieczorek[5], Maria T. Zuber[6], and the GRAIL Science Team. [1]Dept. of Geophysics, Colorado School of Mines, Golden, CO 80401, USA (e-mail: jcahanna@mines.edu); [2]Dept. of Earth, Atmospheric, and Planetary Sciences, Purdue University, West Lafayette, IN, 47907, USA; [3]Dept. of Geological Sciences, Brown University, Providence, RI 02912, USA; [4]NASA Goddard Spaceflight Center, Greenbelt, MD 20771, USA; [5]Institut de Physique du Globe de Paris, 94100 Saint Maur des Fossés, France; [6]Dept. of Earth, Atmospheric and Planetary Sciences, Massachusetts Institute of Technology, Cambridge, MA 02139, USA.

Introduction: Large lunar impact basins are characterized by both their positive central gravity anomalies (mascons) and the presence of multiple ring structures encircling the central depressions. We use data from the Gravity Recovery and Interior Laboratory (GRAIL) mission [1] to more accurately quantify the departures from isostasy associated with the basins and examine the subsurface expressions of the ring structures. An analysis of the isostatic state of the basins demonstrates that the basin structures as a whole are sub-isostatic. Application of the technique of gravity gradiometry to Bouguer-corrected GRAIL gravity data reveals discrete subsurface ring structures surrounding the basins and sheds light on the nature of the rings.

Isostatic state of lunar basins: We define the isostatic anomaly z_{iso} as the height of the surface above or below its theoretical isostatic position [2]. A crustal thickness model [3] was generated from the GRAIL gravity data, assuming a crustal density of 2550 kg/m^3 [4] and applying a cosine taper between degrees 80 and 100. The isostatic anomaly was then calculated, taking into account the effects of membrane stresses arising from the relief on the density interfaces [2]. The global isostatic anomaly map (Figure 1a) reveals the super-isostasy of the centers of the majority of lunar basins, confirming the existence of mascons on both the nearside and farside of the Moon [5]. Each mascon is surrounded by a sub-isostatic annulus in which the surface is below its isostatic elevation. The mean isostatic anomaly was then calculated in the basin center, the surrounding annulus, and the center and annulus together [2]. This analysis reveals that the sub-isostatic annuli overwhelm the super-isostatic mascons, such that the majority of lunar basins are sub-isostatic when averaged over their entire structures. This result is consistent with the theory that the central mascon is caused by the flexural uplift of the outer annulus [2]. We excluded the basins with the thickest mare deposits [6] and examined the remainder for trends in the basin-averaged isostatic anomalies (Figure 1b-c). The isostatic anomalies are found to be most strongly correlated with the basin sizes, with smaller basins being more strongly sub-isostatic. This trend is expected, given the wavelength dependence of the flexural support of lithospheric loads [7]. Correcting for the trend with size, a somewhat weaker correlation is also found with basin age (represented by the number of craters >20 km in diameter [8]), with younger basins exhibiting greater sub-isostasy. This trend can be explained if the isostatic states of the basins were affected by the thermal state of the crust and mantle at the time of impact [9].

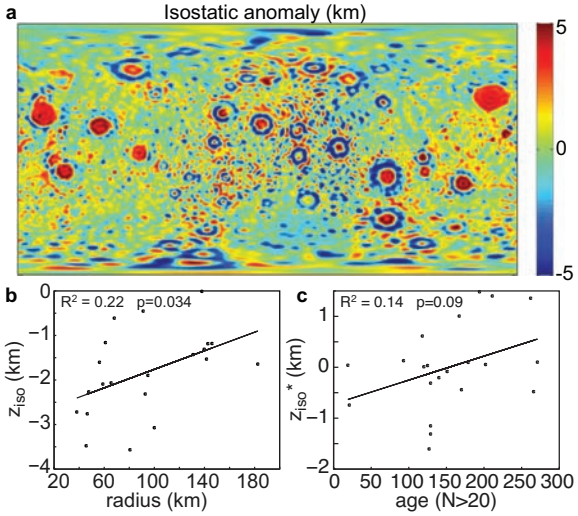

Figure 1. (a) Global isostatic anomaly map, and plots and trend lines of (b) the isostatic anomaly relative to the radius of the central positive Bouguer anomaly, and (c) the isostatic anomaly corrected for radius relative to the basin age [8].

Gravity expression of basin rings: Basin ring structures are characterized by asymmetric scarps and massifs. It has been inferred that some rings continue into the subsurface as discrete fault-like structures. These faults are supported by topographic analyses [10], but direct detection of the subsurface expression of the rings in gravity data was difficult prior to GRAIL [11]. The GRAIL potential model was first divided into terrain (arising from the surface topography) and Bouguer (arising from subsurface density variations) components [1]. High- and low-pass filters were applied at degrees 50 and 300, respectively, and the second horizontal derivatives of the terrain potential ($\Gamma_{T,hh}$) and the Bouguer potential ($\Gamma_{B,hh}$) were calculated [12]. These gradients highlight structures in the topography and subsurface, respectively.

In the Bouguer gravity gradient maps of Crisium and Nectaris (Figure 2c,f), the excavation cavities are outlined by concentric negative and positive rings at the inner and outer edges of the transition zones at the margins of the uplifted mantle plugs. The peak positive Bouguer gradient ring represents the location of maximum upward concavity of the crust-mantle boundary, marking the "rim" of the modified excavation cavity. Outside of the central excavation cavity, ring structures are identified as circular negative gravity gradient anomalies. The subsurface expressions of the rings in the Bouguer gradients are more prominent than their surface expressions in the terrain gradients.

Crisium is surrounded by a strong negative Bouguer gradient ring outside of the rim. The Bouguer gravity data reveals that this ring corresponds with a narrow positive Bouguer anomaly, indicating a positive density anomaly. Image and topography data show that the gravity ring is associated with smooth mare basalt ponded within the outer ring of the basin. These surface mare deposits could also be underlain by dikes intruded into the ring in the subsurface [12].

Nectaris is surrounded by a strong Bouguer gradient ring fully encircling the basin, in contrast to the incomplete topographic ring. Portions of the Bouguer gradient ring are associated with narrow positive Bouguer anomalies. The lack of corresponding surface mare suggests that these anomalies arise from dikes intruded into the ring [12]. In other sections of the ring, the gravity gradients arise from more subtle inflections in the Bouguer gravity. This pattern could arise from tectonic offsets of a subsurface density interface across the ring fault [11]. The ring in the Bouguer gradients is displaced inward relative to that in the terrain gradients by ~130 km. This offset between the surface and subsurface expression of the ring is consistent with an inward dipping fault, but could also reveal the presence of an additional ring between the rim and outer ring.

Conclusions: GRAIL gravity data is leading to significant advances in our understanding of lunar craters and basins at all scales. The long-wavelength signature of the basins shows them to be strongly sub-isostatic as a result of the dominance of the outer sub-isostatic annulus over the inner mascon. Trends in the isostatic anomalies suggest that the isostatic states of the basins are controlled by their sizes and ages. At shorter wavelengths, GRAIL gravity gradients reveal the subsurface expression of basin rings fully encircling the majority of lunar basins. The gravitational signature of the rings appears to result from a combination of mare ponding within surface ring structures, igneous intrusions within ring faults at depth, and tectonic offsets of subsurface density interfaces. Higher-resolution data from the extended mission will better constrain the nature of the rings in the subsurface.

References: [1] Zuber M. T., et al. (2013) *Science* doi: 10.1126/science.1231507. [2] Andrews-Hanna J. C. (2013) *Icarus 222* 159-168. [3] Wieczorek M. A. and Phillips R. J. (1998) *JGR 103* 1715-1724. [4] Wieczorek M. A., et al. (2013) *Science* doi: 10.1126/science.1231530. [5] Neumann G. A., et al. (1996) *JGR 98* 17011-17028. [6] Williams K. K. and Zuber M. T. (1998) *Icarus 131* 107-122. [7] Turcotte D. L., et al. (1981) *JGR. 86*, 3951-3959. [8] Fassett C. I., et al. (2012) *JGR 117* E00H06, doi:10.1029/2011JE003951. [9] Freed A. M., et al. (2013) *LPS 44* [10] Nahm A. L. and Kring D. A. (2011) *LPS 42* Abstract 1172. [11] Kattoum Y. N. and Andrews-Hanna J. C. (2012) *LPS 43* Abstract 2767. [12] Andrews-Hanna J. C., et al. (2013) *Science* doi:10.1126/science.1231753.

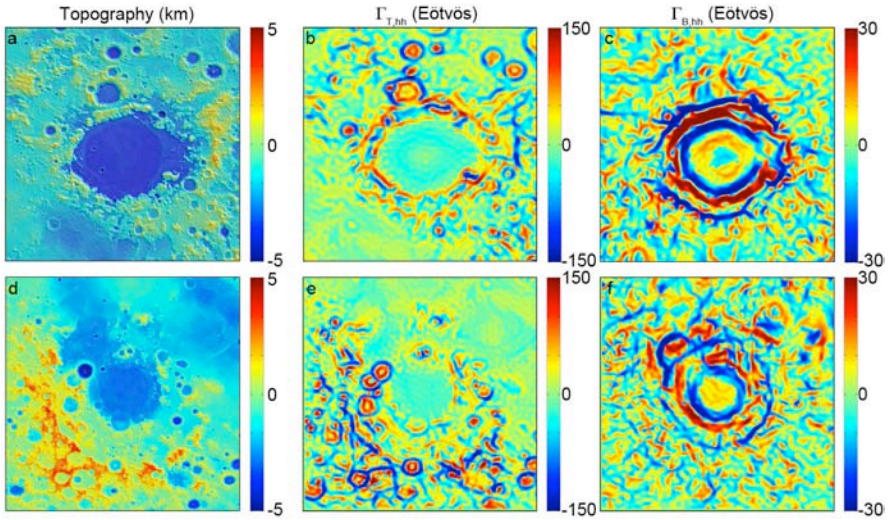

Figure 2. Topography, terrain gravity gradients ($\Gamma_{T,hh}$), and Bouguer gravity gradients ($\Gamma_{B,hh}$) for (a-c) Crisium and (d-f) Nectaris. The gravity gradients are in units of Eötvös (1 $E = 10^{-9}$ s^{-2})